Collision Dynamics and Internal Mixing of Droplets of Non-Newtonian Liquids

Kai Sun,[1,2] Peng Zhang,[3,*,†] Chung K. Law,[4,2,*,‡] and Tianyou Wang[1]

[1]*State Key Laboratory of Engines, Tianjin University, Tianjin 300072, China*
[2]*Department of Mechanical and Aerospace Engineering, Princeton University, Princeton 08544, New Jersey, USA*
[3]*Department of Mechanical Engineering, Hong Kong Polytechnic University, Hong Kong 999077, China*
[4]*Center for Combustion Energy, Tsinghua University, Beijing 100084, China*

(Received 7 February 2015; revised manuscript received 7 June 2015; published 24 November 2015)

The efficient internal mixing of colliding droplets upon coalescence is critical to various technological processes such as color manipulation in ink-jet printing and the initiation of the liquid-phase reaction of gelled hypergolic propellants in rocket engines. Recognizing that such processes can be optimized by varying the impact inertia as well as employing fluids of non-Newtonian rheology, the head-on collision, coalescence, and internal mixing pattern between two *impacting* equal-sized droplets of *non-Newtonian* fluids is computationally investigated by using the lattice Boltzmann method. Results show that, with increasing non-Newtonian effects, droplet deformation and separation following coalescence is promoted for shear-thinning fluids, while permanent coalescence allowing an extended duration for mixing is promoted for shear-thickening fluids. Furthermore, large-scale internal mixing is promoted for the colliding droplets with larger shear-thinning disparity, while coalescence and mixing is synergistically facilitated for the collision between a shear-thinning droplet and a shear-thickening droplet. The individual and coupled influences of viscosity on the droplet deformation and impact inertia, internal motion, viscous loss, and merging of the colliding interfaces leading to the observed outcomes are mechanistically identified and described.

DOI: 10.1103/PhysRevApplied.4.054013

I. INTRODUCTION

Droplet collision in a gaseous environment is of relevance to many natural and industrial processes such as raindrop and cloud formation, ink-jet printing, spray coating, and spray combustion. As such, substantial experimental [1–7], numerical [8–11], and theoretical investigations [12–15] have been conducted to unravel the rich physics involving either droplet-droplet collision or droplet impaction on a dry or wetted surface, leading to the occurrence of such non-monotonic global outcomes as bouncing, permanent coalescence, and separation subsequent to temporary coalescence, as the impact inertia increases. Recently, internal mixing of colliding droplets upon coalescence has gained considerable interest [16–22], especially for its practical relevance in the control and design of such technological processes as color manipulation in ink-jet printing [23,24], facilitated liquid-phase reaction in propulsion systems utilizing gelled hypergolic propellants [25,26], and property design in materials synthesis [27,28].

Mechanistically, since the extent of internal mixing is minimal for the head-on collision of two *identical* droplets due to the intrinsic symmetry across the plane of collision, efficient mixing must require breaking the collision symmetry by instituting disparities in either the size [16–20] and/or the rheological properties of the colliding droplets, such as the surface tension [21] and viscosity [22]. It is noted that the fuel and the oxidizer are actually non-Newtonian fluids in gelled hypergolic propellants (GHP), which are promising fuels for next-generation missile and rocket engines, while most previous studies on droplet collision have used Newtonian fluids. It thereby behooves us to investigate and thereby exploit the collision response of non-Newtonian fluids, which can be highly nonlinear and even trend reversing [29] but are much less understood than Newtonian fluids. In this regard, we note that Motzigemba *et al.* [30] experimentally found that the deformation of colliding droplets of shear-thinning fluids is substantially larger than that of the Newtonian fluid, while Focke and Bothe [31,32] numerically found that the collision dynamics of non-Newtonian droplets can be reproduced by that of Newtonian droplets with an effective viscosity. We recognized that droplet collision and internal mixing can become extremely complicated by considering the influence of the Weber number (We), the Ohnesorge number (Oh), the size ratio, and the non-Newtonian rheology. In a previous work [33], we consider a simplified yet physically meaningful problem of *momentumless* droplet coalescence of shear-thinning fluids in order to isolate the effects of rheology from those of impact inertia. It was observed that the coalescence between a Newtonian and a non-Newtonian droplet of the *same size* results in unsymmetrical, albeit small, mixing due to the momentum imbalance induced by the shear-thinning effect.

*To whom all correspondence should be addressed.
†pengzhang.zhang@polyu.edu.hk
‡cklaw@princeton.edu

Specifically, droplet coalescence is accompanied by the conversion of the surface energy of the merging interface into the kinetic energy of the internal motion, which is simultaneously and locally affected by viscous dissipation. Because of the reduced local viscosity and thereby smaller viscous dissipation for shear-thinning fluids, the flow in the non-Newtonian droplet is faster than that in the Newtonian droplet. As a result, the non-Newtonian liquid with a higher kinetic energy wedges unto the Newtonian droplet from the outer edge of the contact surface and eventually wraps around the Newtonian droplet. The above findings are encouraging since the droplet internal motion is driven solely by the surface tension of the *initially stationary* droplets, and the local shear rate remains small and mixing through non-Newtonian effects is limited. Consequently, it motivates us to expect that, for *colliding* droplets, non-Newtonian effects on enhancing internal mixing can be substantially augmented because of the correspondingly substantial internal motion generated through the impact inertia [31].

In view of the above considerations, we comprehensively investigate the internal mixing dynamics of head-on *colliding* droplets of non-Newtonian fluids for a wide range of We numbers, up to O(100). Furthermore, we allow the non-Newtonian effect to be either shear thinning or shear thickening, and thereby demonstrate the richness in the efficiency of internal mixing through manipulation of the rheological properties. Among the four possible outcome regimes of head-on droplet collision [3], namely, (i) coalescence with minor deformation, (ii) bouncing, (iii) coalescence with large deformation, and (iv) reflexive separation, we shall focus on only regimes (iii) and (iv). This is because regime (i) is similar to that of the merging of initially stationary droplets [33], while regime (ii) occurs only within a relatively narrow range of We and does not result in any substantial droplet mixing.

In the following, the numerical methodology, results and discussion, and concluding remarks are sequentially presented in Secs. II through IV.

II. NUMERICAL METHODOLOGY

Since head-on droplet collision is intrinsically symmetric with respect to the axis connecting the centers of mass of the two droplets, the computation domain is axisymmetric, with droplets of diameter D initially spaced $2D$ apart and with an equal velocity of $U/2$ in opposite directions, as shown in Fig. 1. The Neumann boundary condition of zero gradients for all the variables is applied on the domain boundaries except the axis.

The lattice Boltzmann method (LBM) [34,35] is used to solve the droplet dynamics, with the mixing process visualized by tracking massless particles in the droplets by using the fourth-order Runge-Kutta method. Among the sophisticated LBM multiphase models developed in recent years [36–40], the phase-field model proposed by Lee *et al.* [39,40] is employed in the present study. By implementing the potential form of surface tension and isotropic finite difference, this model is able to suppress the well-known spurious current at a relatively low level even for high density ratios [39,40]. To account for non-Newtonian fluid effects, all the viscosity-related terms, including the relaxation parameters in the collision matrix and other terms in the evolution equations, are replaced by the shear-rate dependent viscosity once the local fluid is identified to be non-Newtonian by the tracking particles in every time step. Details of the numerical method are given in Refs. [19,33].

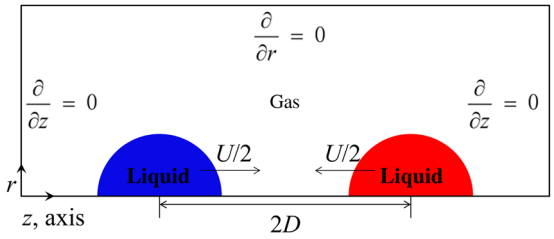

FIG. 1. Specifications of computational domain and boundary conditions.

Both shear-thinning and shear-thickening fluids are considered. The Carreau-Yasuda (CY) model is used to model the shear-thinning fluids:

$$\mu(\dot{\gamma}) = \mu_\infty + (\mu_0 - \mu_\infty)[1 + (\lambda_{\mathrm{CY}}\dot{\gamma})^a]^{(n-1)/a}, \quad (1)$$

where μ_0 and μ_∞ are the dynamic viscosity at zero and infinite shear rates, respectively; λ_{CY} is a time constant; n is a power-law index; and a is a parameter affecting the transition between the zero-shear rate and power-law regimes [41]. To model shear-thickening fluids, which are well known to exhibit shear-thickening rheology at intermediate shear rates and shear-thinning rheology at high and low shear rates [42], a piecewise function is defined:

$$\mu(\dot{\gamma}) = \begin{cases} \mu_0, & \dot{\gamma} \le \dot{\gamma}_{c,1} \\ \mu_0 \dot{\gamma}^{n_1-1}, & \dot{\gamma}_{c,1} < \dot{\gamma} \le \dot{\gamma}_{c,2} \\ \mu_0 \dot{\gamma}_{c,2}{}^{n_1-1}/[1 + (\dot{\gamma} - \dot{\gamma}_{c,2})^{1-n_2}], & \dot{\gamma} > \dot{\gamma}_{c,2}, \end{cases} \quad (2)$$

in which $\dot{\gamma}_{c,1}$ and $\dot{\gamma}_{c,2}$ are the critical shear rates, and n_1 and n_2 are the power-law indexes. Since the characteristic shear rates (U/D) in the present study are generally of $\mathrm{O}(10^4)$ s^{-1} and our simulation results show little relevance with low shear rates of $\mathrm{O}(1)$ s^{-1}, the fluid viscosity is assumed to be constant rather than shear thinning in the region of $\dot{\gamma} \le \dot{\gamma}_{c,1}$ for simplicity.

Noting that the present numerical methodology is not restricted to any specific non-Newtonian fluid, Eqs. (1) and (2) are adopted only as representative models to describe shear-thinning and shear-thickening effects. For the

parameters in Eqs. (1) and (2), μ_0 and μ_∞ are implicitly determined by the Ohnesorge number, which is specified as a varying parameter in the study, and λ_{CY}, a, n, n_1, n_2, $\dot{\gamma}_{c,1}$, and $\dot{\gamma}_{c,2}$ are related to the extent of the non-Newtonian flow effect. In Ref. [33], $\lambda_{CY} = 61.9\ T_{osc}$ where $T_{osc} = (\pi/4)\sqrt{\rho_l R^3/\sigma}$ is the characteristic oscillation time of the droplet, and $a = 0.557$ and $n = 0.5$ correspond to a typical carboxymethyl cellulose solution (CMC) [41]. The parametric study shows that λ_{CY} and n have a similar and quantitatively moderate influence on droplet coalescence and internal mixing [33]. Consequently, for simplicity $\lambda_{CY} = 1000\ T_{osc}$ and $a = 0.557$ are kept as constants in all of the simulations, and only n is varied to mimic the different extents of shear-thinning effects. λ_{CY} is increased so that the shear-thinning effect can be more prominently demonstrated through n. For shear-thickening fluids, the critical shear rates $\dot{\gamma}_{c,1}$ and $\dot{\gamma}_{c,2}$ are chosen to be 1 s^{-1} and 1000 s^{-1}, respectively, according to the typical values of real shear-thickening fluids [42], $n_2 = 0.8$ is kept as a constant, and n_1 is varied to realize the different extent of the shear-thickening effect. In addition, in order to quantify the extent of the non-Newtonian flow effect, n' is defined as $n' = 1 - n$ for shear-thinning fluids and $n' = n_1 - 1$ for shear-thickening fluids, with larger n' corresponding to the stronger non-Newtonian flow effect.

The colliding droplets, while possessing different non-Newtonian flow effects, are assumed to have identical density ρ_l and surface tension σ. In addition, dilution of the non-Newtonian flow effect through mass diffusion is neglected because the Peclet number is generally up to $O(10^5)$ if the characteristic velocity and length are chosen to be the relative velocity of the droplets and the droplet diameter, respectively.

It is further noted that droplet collision at nonvanishing We spans a wide range of scales, particularly those relevant for the intervening gas flow between the impacting surfaces and their subsequent merging triggered by the van der Waals force [12]. The occurrence of coalescence then depends on whether or not the clearance between the impacting surfaces can reach a critical range of distance before the droplets lose their impact inertia. Within the critical range of typically tens of nanometers, the van der Waals force gradually dominates over other forces and eventually causes the interfaces to merge. The gas-film thickness could vary by 3–4 orders of magnitude during this final stage of transition, and is beyond the present computational capacity for resolution.

With the above considerations, and following the common numerical treatment for many interface-capturing methods such as volume of fluid and level set methods, the artificial resolution of the gas-liquid interface on a few mesh grids is used. It is further noted that the main idea of the present LBM multiphase model actually stems from the phase-field method, which employs a phase-field variable to represent the concentration of the entire field [19,39,40]. Based on minimizing the free energy, the phase-field variable satisfies the Cahn-Hilliard equation, and the interfacial dynamics can be automatically captured without any artificial treatment. When two interfaces are sufficiently close to each other, an attractive force will develop automatically by the free energy to trigger the interface coalescence. Therefore, the phase-field method can be considered as a subgrid model to account for the physics of short-range molecular force, which occurs at much smaller scales [43,44].

In terms of the numerical resolution in the present study, the diffuse interface in LBM simulation is kept to 5 lattice spacing, and the droplet diameter is set at 200 lattice spacing to produce grid-independent results. Furthermore, sufficient tracking particles, i.e., 5 per lattice spacing in both axial and radial directions, are added in the droplets to visualize the mixing process. A typical simulation with the computational domain of $1.5D$ (radial) $\times$ $5D$ (axial) generally takes 100–150 hours on an Intel 2.67 GHz Westmere CPU. It is emphasized that although the present resolution is insufficient to resolve the intervening gas flow, the key physics during the drainage and coalescence process is included in the simulation. This physics involves two competitive effects, namely the pressure rise in the gap tending to repel the droplets, and the attraction forces generated from free energy tending to attract the interfaces. Moreover, as Chiappini *et al.* [45] demonstrated, the lack of mass conservation of the present model is very minor and produces negligible effects, and as such the mass of the droplets is well conserved in all the tested cases of the present study. The maximum magnitude of the spurious current, which can only be evaluated through static droplet test, is on the order of 10^{-5} in lattice unit and is significantly smaller than the characteristic velocity of the problem, where the relative velocity between the droplets is generally on the order of 10^{-2} in lattice unit. Therefore, the effect of the spurious current is believed to be negligible in the present study.

III. RESULTS AND DISCUSSION

For equal-sized droplet collision in a gaseous environment, the controlling parameters are the We number, $We = \rho_l U^2 D/\sigma$, and the Oh number, $Oh = \mu_l/\sqrt{\rho_l \sigma D}$. Since the viscosity of non-Newtonian fluid is not constant, the Ohnesorge number is based on the viscosity at zero shear rate, while the effective Oh number Oh_{eff} is defined based on the viscosity at the characteristic shear rate $\dot{\gamma}_c = U/D$ for comparison of different shear-rate-dependent cases. In addition, time is nondimensionalized through $T = tU/D$. Furthermore, the density and viscosity of the gas are those of atmospheric air so that the liquid-gas density and viscosity ratios are too large to have any significant influence on the droplet deformation [5,12], and as such their effects will not be studied.

A. Experimental verification

The present numerical methods have been validated for droplet coalescence including internal mixing at small We [33]. To further validate the numerical method, simulation is first conducted on Newtonian droplet collision at large We. Figure 2 compares the simulation and experimental [3] results of tetradecane droplet collision at $\mathrm{Oh} = 0.0265$ and $\mathrm{We} = 37.2$. This particular case is chosen because it is close to the boundary between coalescence and reflexive separation, with the prominent feature of the generation of a satellite droplet after separation occurs. As shown in Fig. 2, the simulation agrees quantitatively well with the experiment in both the droplet deformation and the satellite droplet generation. An interesting observation is that a small bubble is trapped in the coalesced mass at $T = 0.77$, which indicates that interface merging takes place at the circular rim rather than at the center. The bubble gradually disappears and is no longer observed at $T = 2.03$ since it is too small to be preserved from unavoidable numerical dissipation.

The above observation substantiates the adequacy of the present method in resolving the intervening gas flow and capturing the essential characteristics of droplet coalescence at large We. It is also noted that successfully capturing the bubble entrapment upon droplet coalescence usually demands extremely fine mesh for VOF- or level-set-based simulation methods.

To further validate the method in simulating the collision of non-Newtonian droplets, the experimental results by Motzigemba *et al.* [30] are compared. As shown in Fig. 3(a), the measured viscosity of the CMC water solution fits well with the modified power law as $\mu(\dot{\gamma}) = \mu_0/(1+\mu_0\dot{\gamma}^{1-n}/K)$, in which $\mu_0 = 0.095$ Pa s, $n = 0.77$, and $K = 1.17$. As shown in Fig. 3(b), the present simulation agrees reasonably well with the experiment in the early, radial expansion stage ($T < 8$) of droplet deformation as well as the state of the maximum deformation. However, droplet deformation at the late, radial recession stage ($T > 8$) is overshot numerically even if accounting for the 10% uncertainty in the experimental measurement of the initial droplet diameter. It is noted that the VOF simulation by Focke and Bothe also shows significant deviation from the experiment [31]. Their explanation of the deviation is that the measurement of the droplet

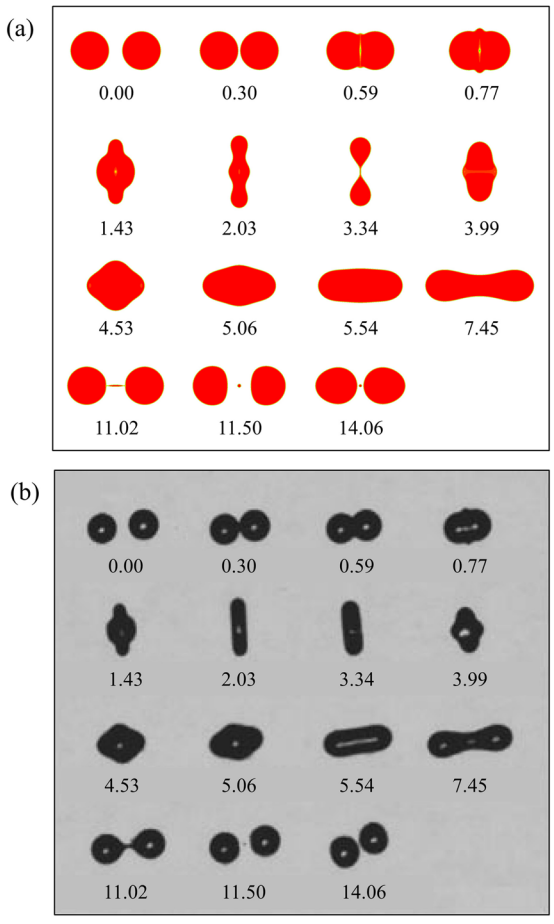

FIG. 2. Experimental verification of Newtonian (tetradecane) droplet collision at $\mathrm{Oh} = 0.0265$ and $\mathrm{We} = 37.2$: (a) simulation; (b) experiment [3].

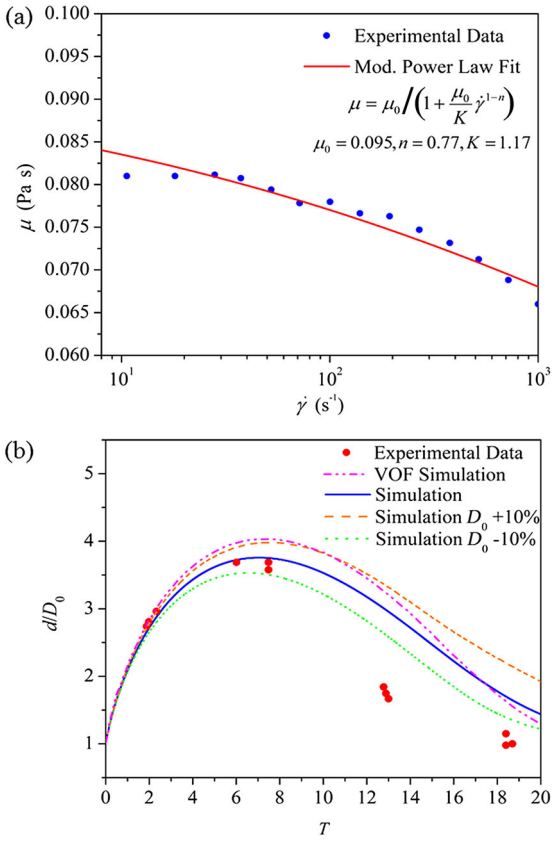

FIG. 3. Experimental verification of non-Newtonian (CMC water solution) droplet collision at $\mathrm{Oh} = 0.565$, $\mathrm{We} = 766$: (a) experimental values and fit-curve of the liquid viscosity; (b) comparison of the simulation and experiment on the radial deformation. The experimental data are extracted from Refs. [30,31], and the VOF simulation result is extracted from Ref. [31].

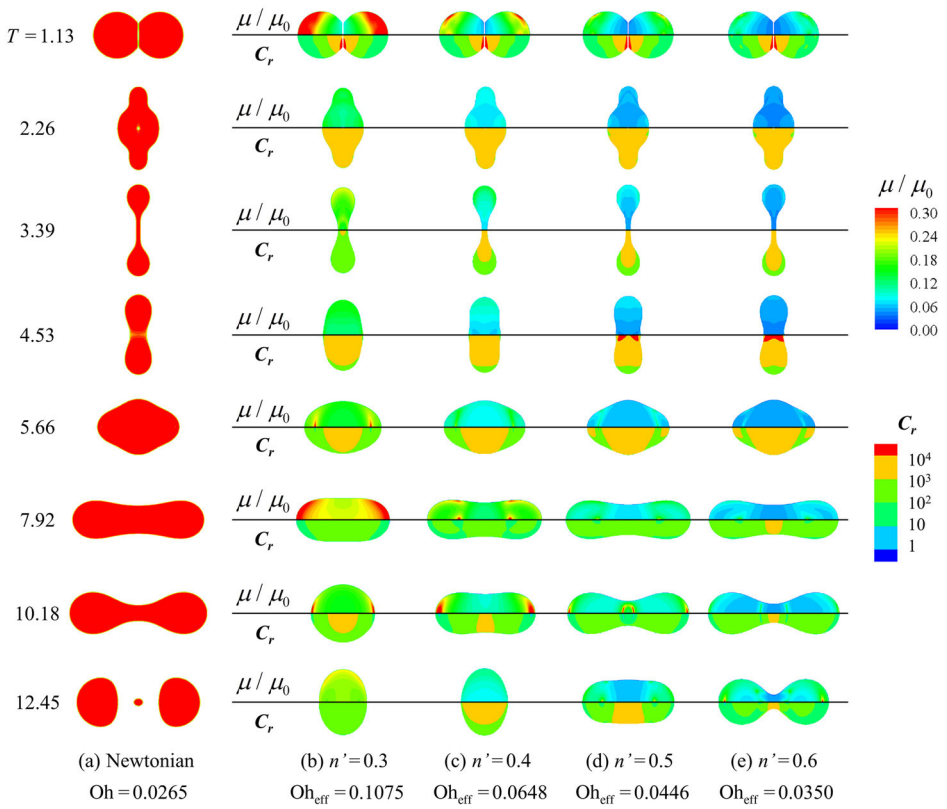

FIG. 4. Comparison of droplet collision of Newtonian and shear-thinning fluid at We = 40: (a) Newtonian fluid, Oh = 0.0265; (b)–(e): shear-thinning fluid, Oh = 0.795, $Oh_\infty = 0.0265$, (b) $n' = 0.3$, $Oh_{eff} = 0.1075$, (c) $n' = 0.4$, $Oh_{eff} = 0.0648$, (d) $n' = 0.5$, $Oh_{eff} = 0.0446$, (e) $n' = 0.6$, $Oh_{eff} = 0.0350$.

deformation during the radial recession stage may be underestimated due to rotation of the droplet in the experiment, as shown in Fig. 2(b) in Ref. [30].

Having largely validated the computational results against the experiments on the deformation of colliding non-Newtonian droplets [30] as well as on the collision dynamics [19] and internal mixing [33] of Newtonian droplets, we proceed with reasonable confidence with the simulation of the collision and internal mixing dynamics of non-Newtonian droplets.

B. Collision of identical droplets of shear-thinning fluid

We first study the collision of droplets of shear-thinning fluid. Figure 4 shows the time sequence of droplet collision at We = 40, in which case (a) is for Newtonian fluid as the benchmark, and cases (b)–(e) are non-Newtonian fluids with a different extent of shear thinning. For the benchmark case (a), the Ohnesorge number is set as Oh = 0.0265 in accordance with the tetradecane experiment of Qian and Law [3]. For the shear-thinning cases (b)–(e), it is set as Oh = 0.795, which is 30 times larger than that of case (a) because shear-thinning non-Newtonian fluids are usually much more viscous than Newtonian fluids in quiescence; the local viscosity and the Carreau-number ($Cr = \dot{\gamma}\lambda_{CY}$) distributions are plotted on the upper and lower halves of the subfigures, respectively. It is seen that, for the non-Newtonian fluid with the least shear-thinning effect [case (b), $n' = 0.3$, $Oh_{eff} = 0.1075$], droplet deformation is greatly suppressed by viscous dissipation due to the significantly higher initial viscosity compared with the Newtonian fluid. With the increasing extent of shear thinning, the shear rate of the droplet internal motion becomes increasingly effective in reducing the local viscosity, and the droplet tends to deform more substantially. Besides, the Cr number is generally much larger than unity during the entire process of droplet collision, indicating that the non-Newtonian flow effect, rather than simply viscosity, always plays a role in the present problem.

For the final outcome of droplet collision, permanent coalescence is preferred to facilitate droplet mixing. When reflexive separation occurs, mixing is possible only within the satellite droplet because of symmetry, as the case shown in Fig. 4(a). For cases (b)–(e), the promotion of permanent coalescence is the result of increased viscosity instead of shear thinning, which shows only a moderate influence on droplet deformation at We = 40.

To further quantify the shear-thinning effect on the boundary separating coalescence and reflexive separation, a parametric study is conducted for $0.3 \le n' \le 0.6$. In Fig. 5(a), for which Oh_∞ equals to the Oh of the benchmark Newtonian fluid, the dashed line, representing the critical transition We for the non-Newtonian droplets, lies above the dotted horizontal line, which represents $We_{Cr} = 36$ of the Newtonian droplets. This indicates that reflexive separation of non-Newtonian droplets is harder to occur than that of Newtonian droplets as long as shear thinning is not sufficiently strong to substantially reduce Oh_∞. Furthermore, if shear thinning is strong enough, as shown

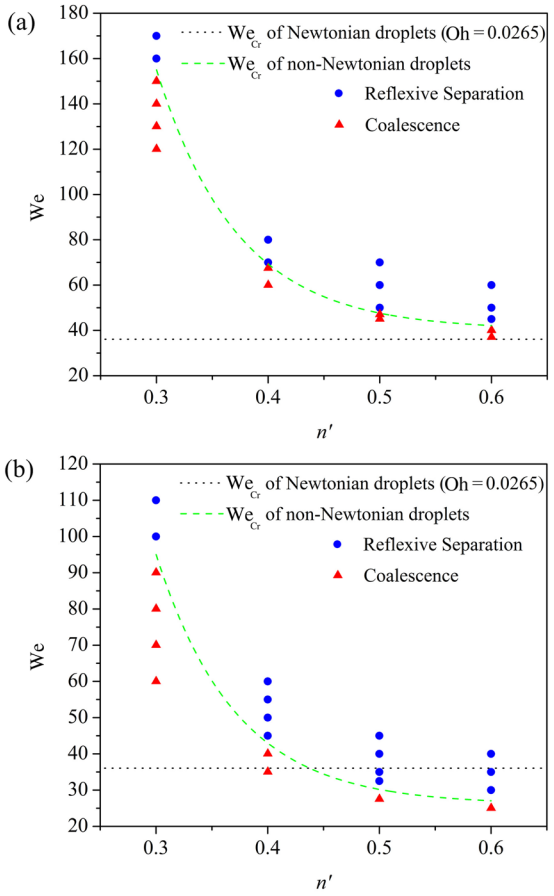

FIG. 5. The outcome of non-Newtonian droplet collision with a different extent of the shear-thinning effect: (a) Oh = 0.795, $\mathrm{Oh}_\infty = 0.0265$; (b) Oh = 0.795, $\mathrm{Oh}_\infty = 0.002$.

in Fig. 5(b) where Oh_∞ can be reduced to be smaller than the Newtonian Oh = 0.0265, the non-Newtonian droplet can even separate at smaller We. This result suggests that highly shear-thinning propellants should be avoided in GHP rocket engines because coalesced fuel-oxidizer droplets of a high shear-thinning effect tend to separate easily.

C. Collision of droplets of different shear-thinning fluids

Considering that large-scale internal mixing for the identical droplet collision is inherently inhibited by symmetry, disparity in shear thinning may break the symmetry to facilitate internal mixing. Figure 6 shows the collision of droplets of the same size but different shear-thinning fluids, in which the "blue" droplet has a stronger shear-thinning effect ($n' = 0.6$) than the red one ($n' = 0.4$), with other physical properties remaining identical, as Oh = 0.795, $\mathrm{Oh}_\infty = 0.002$. It is seen that for case (a) with a relatively small We = 20, the droplets stay pernamently coalesced with the blue droplet wrapping around the red one. Compared with the cases of identical droplets, the region bounded by the liquid-liquid contact surface is substantially enlarged, especially during the axial deformation period of $T = 4.80$–8.40. With a further increase of the impact inertia, reflexive separation starts even at We = 40 due to shear thinning. However, mixing is also significantly improved due to symmetry breaking so that the colliding droplets have penetrated into each other. Take case (b) for instance: after separation at $T = 12.73$, the mass fraction from the original red droplet is 20.4%, 59.4%, and 80.2% (from left to right) in the three child droplets, respectively.

To further quantify the extent of mixing, a local mixing index at each grid point (x_0, y_0) is defined by

$$\phi = \frac{N_R}{N_R + N_B} = \begin{cases} 0, & \text{if mass from the blue droplet} \\ 0\text{–}1, & \text{if mass from both droplets} \\ 1, & \text{if mass from the red droplet,} \end{cases} \tag{3}$$

in which N_R and N_B are the number of tracking particles within a grid cell, i.e., $(x_0 - \Delta x/2) \le x < (x_0 + \Delta x/2)$, $(y_0 - \Delta y/2) \le y < (y_0 + \Delta y/2)$, from the red and blue droplets, respectively. Since mixing occurs only for $0 < \phi < 1$ and maximizes at $\phi = 0.5$, a global mixing intensity can be defined as [46]

$$\Phi = 1 - \sqrt{\frac{\int (2\phi - 1)^2 dV}{V}}, \tag{4}$$

where the second term on the rhs of Eq. (4) represents the covariance of ϕ over the droplet volume V. Consequently, the mixing intensity of the colliding droplets shown in Fig. 6(b) can be compared with that of a pair of colliding droplets with $\mathrm{Oh}_{\mathrm{eff}} = 0.0262$ and identical shear-thinning effect $n_1' = n_2' = 0.5344$. As shown in Fig. 7, after the droplets coalesce at $tU/D \approx 1.0$, the mixing intensity increases with the radial expansion of droplet contact area, showing little difference for the two cases during this stage. However, as the merged droplet recedes after maximum deformation, the facilitation by symmetry breaking on internal mixing becomes prominent as the result of the enhanced mass interpenetration. Therefore, if the fuel and the oxidizer are gelled with a different extent of shear thinning, the ignition of GHP rocket engines could be facilitated because even though the coalesced fuel-oxidizer mass would finally separate, the child droplets can still be well mixed.

To unravel the underlying physics of the above result, the evolution of the flow field and the viscosity distribution of case (b) in Fig. 6 is chosen for further study. As shown in Fig. 8, the droplet collision process can be divided into three stages, respectively, corresponding to radial expansion ($T < 2.83$), radial recession ($T = 2.83$–4.53), and axial elongation ($T > 4.53$). Specifically, during the radial expansion stage, the coalesced droplet is driven by the axial counterflow, and the viscosity in the blue liquid is reduced more by the stronger shear-thinning effect. Therefore, the

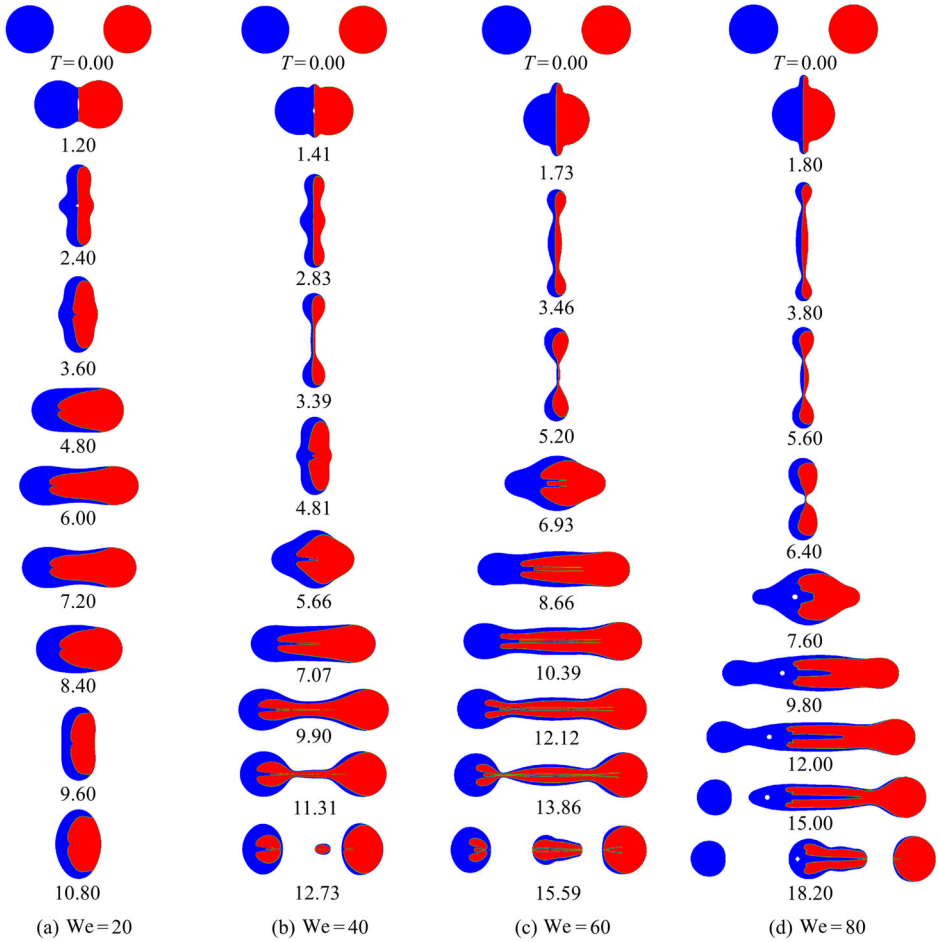

FIG. 6. Droplet collision of different shear-thinning fluids (blue droplet: $n' = 0.6$, $\mathrm{Oh_{eff}} = 0.0415$; red droplet: $n' = 0.4$, $\mathrm{Oh_{eff}} = 0.0108$) at $\mathrm{Oh} = 0.795$, $\mathrm{Oh}_\infty = 0.002$: (a) $\mathrm{We} = 20$; (b) $\mathrm{We} = 40$; (c) $\mathrm{We} = 60$; (d) $\mathrm{We} = 80$.

blue liquid tends to wedge slightly into the red one from the radial rim ($T = 1.70$), as the result of smaller viscous dissipation and larger flow momentum in the blue liquid. As the droplet further expands and then recedes, wedging penetration of the blue liquid around the rim keeps growing and becomes sufficiently manifest in the radial recession stage ($T = 3.68$). It is also noted that, in the present axisymmetric computational domain, even a visibly slight mixing in the rim corresponds to considerable amount of mass exchange. Therefore, during the axial elongation stage, the mixing becomes increasingly prominent as the droplet stretches, and finally results in the well-mixed child droplet after separation occurs.

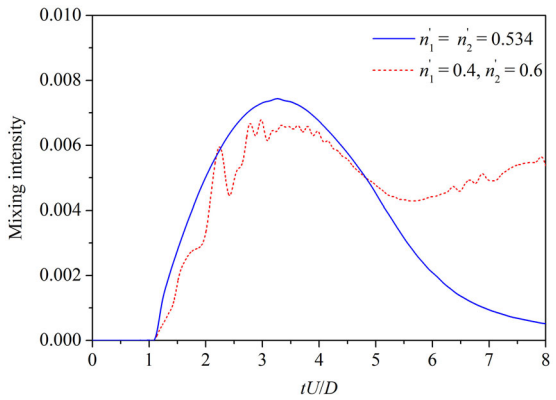

FIG. 7. Comparison of the mixing intensity between colliding droplets with idential shear-thinning effect ($n_1' = n_2' = 0.5344$, $\mathrm{Oh_{eff,1}} = \mathrm{Oh_{eff,2}} = 0.0262$) and with different shear-thinning effect ($n_1' = 0.6, \mathrm{Oh_{eff,1}} = 0.0108$; $n_2' = 0.4, \mathrm{Oh_{eff,2}} = 0.0415$) at $\mathrm{We} = 40$.

D. Collision of identical droplets of shear-thickening fluid

We next consider the collision of identical droplets of shear-thickening fluid. Figure 9 shows the collision sequence for $\mathrm{We} = 100$ and $\mathrm{Oh} = 0.1$. For Newtonian droplet collision at the same Ohnesorge number, the critical Weber number separating the coalescence and separation regimes is around 80 [3]. For shear-thickening fluid, the droplet deformation is significantly suppressed due to the increasing viscous dissipation with the extent of shear thickening. Even at the low shear-thickening effect of $n' = 0.1$, reflexive separation does not occur at $\mathrm{We} = 100$. As this effect increases, separation is hardly possible since the excessive kinetic energy of the droplet internal motion is rapidly dissipated during the radial deformation stage. Extensive simulation shows that reflexive separation does not occur up to $\mathrm{We} = 500$ for the case of $n' = 0.3$. Consequently, shear-thickening fluid holds

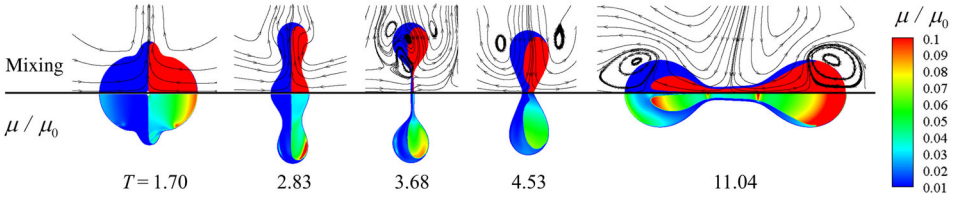

FIG. 8. Evolution of the flow field and the normalized viscosity distribution of case (b) in Fig. 6.

potential in promoting the permanent coalescence of colliding droplets, although the "wedging" motion of the droplets is not likely to happen with significant viscous stress.

E. Droplet collision of shear-thinning and shear-thickening fluids

In view of the above result that, upon collision, the disparity in the shear thinning promotes strong mixing by breaking the symmetry while that of shear thickening tends to retain coalescence, it is then of interest to explore whether the collision between a shear-thinning droplet and a shear-thickening droplet could simultaneously suppress separation and facilitate mixing. In order to demonstrate the distinct difference in the non-Newtonian flow effect and the high viscous dissipation in the shear-thickening fluid at the same time, we have adopted a strong shear-thinning droplet with $\mathrm{Oh}_\infty = 0.002$ and $n' = 0.6$, and a strong shear-thickening droplet with $n' = 0.3$, while keeping their Oh number the same, at $\mathrm{Oh} = 0.1$.

As shown in Fig. 10, the collision between the shear-thinning and shear-thickening droplets does result in the simultaneous suppression of separation and enhanced mixing. It is seen that even though the droplet sizes are the same, symmetry is broken to a larger extent than the cases involving different shear-thinning fluids, shown in Fig. 6. During the radial expansion stage, the shear-thinning droplet tends to spread extensively over the shear-thickening droplet, forming a concavity on the shear-thickening droplet side [e.g., $T = 4.38$ in Fig. 10(c)]. During the stages of radial recession and axial elongation, droplet deformation is substantially suppressed due to the presence of the shear-thickening fluid, and reflexive separation occurs only on the side of the shear-thinning fluid as We exceeds 200.

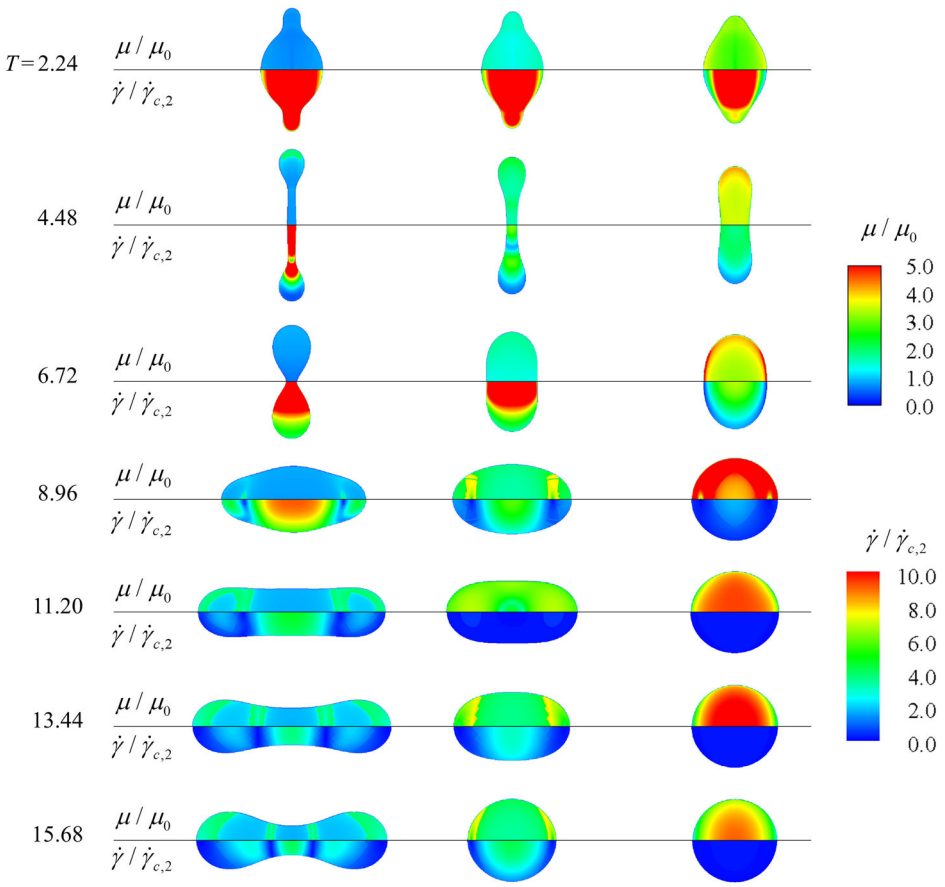

(a) $n' = 0.1$, $\mathrm{Oh}_{\mathrm{eff}} = 0.078$ (b) $n' = 0.2$, $\mathrm{Oh}_{\mathrm{eff}} = 0.155$ (c) $n' = 0.3$, $\mathrm{Oh}_{\mathrm{eff}} = 0.309$

FIG. 9. Droplet collision of identical shear-thickening fluids at $\mathrm{Oh} = 0.1$ and $\mathrm{We} = 100$: (a) $n' = 0.1$, $\mathrm{Oh}_{\mathrm{eff}} = 0.078$; (b) $n' = 0.2$, $\mathrm{Oh}_{\mathrm{eff}} = 0.155$; (c) $n' = 0.3$, $\mathrm{Oh}_{\mathrm{eff}} = 0.309$.

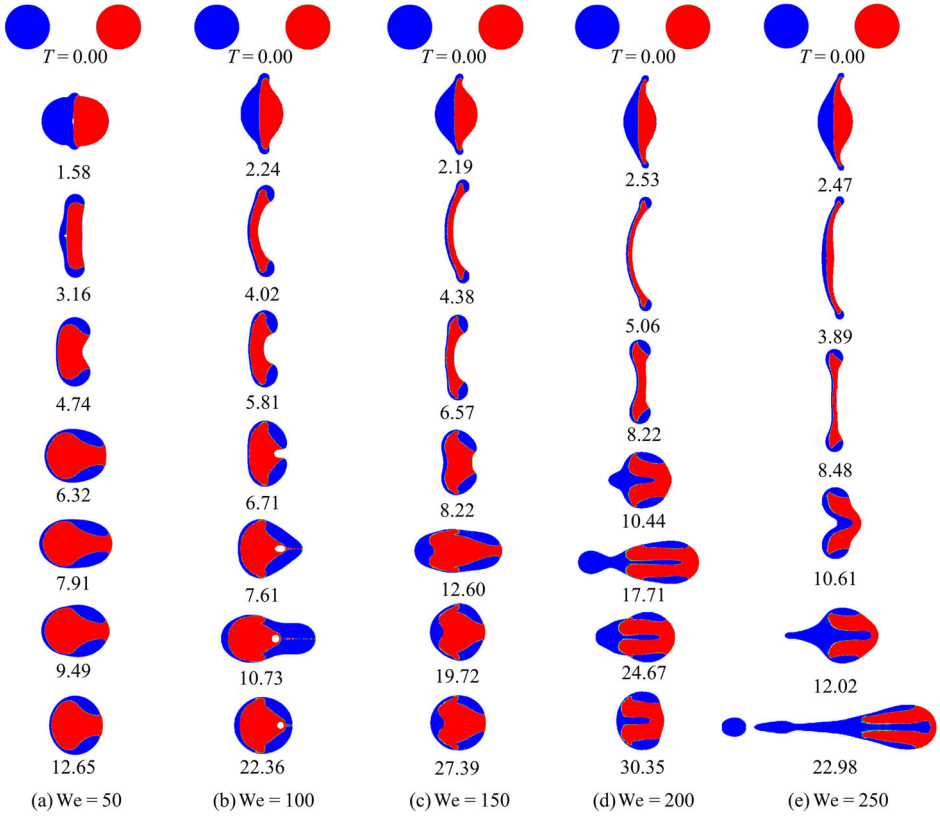

FIG. 10. Collision between a shear-thinning droplet (blue, $\mathrm{Oh} = 0.1$, $\mathrm{Oh}_\infty = 0.002$, $n' = 0.6$) and another shear-thickening droplet (red, $\mathrm{Oh} = 0.1, n' = 0.3$): (a) $\mathrm{We} = 50$; (b) $\mathrm{We} = 100$; (c) $\mathrm{We} = 150$; (d) $\mathrm{We} = 200$; (e) $\mathrm{We} = 250$.

In terms of internal mixing in the coalesced mass, it is of interest to observe the nonmonotonic regimes of partial wrap up, full entrapment, and partial wrap up again with increasing We. Specifically, at relatively low We [Fig. 10(a)], the axial concavity is shallow and is able to restore quickly; consequently the shear-thinning droplet just partially wraps up the shear-thickening one. At higher We [Fig. 10(b)], radial expansion is more significant and the concavity is deeper. During the radial recession stage, the restoration of the axial concavity on the shear-thickening side is slower due to substantial viscous damping, while that on the shear-thinning side is much faster so that the shear-thinning fluid wraps up the entire shear-thickening fluid. Extensive simulation shows that this phenomenon of confluent shear-thinning fluid occurs at a wide range of $\mathrm{We} = 75$–125. By further increasing We [Figs. 10(c)–10(e)], the droplet expands more widely in the radial direction, and the axial concavity is able to be restored while the radial rim is still shrinking. Consequently, the shear-thickening fluid can no longer be fully wrapped up by the shear-thinning fluid.

However, different from the partial wrap-up regime at relatively low We, the fluids interpenetrate remarkably in the partial wrap-up regime at higher We. As shown in Fig. 11, during the radial expansion stage, the distinct disparity in the non-Newtonian flow effect causes the highly nonuniform viscosity distribution of the fluids. Because of the greatly reduced viscous dissipation and thereby the associated higher momentum, the shear-thinning fluid not only wedges into the shear-thickening fluid from the outer edge, but it also drives the shear-thickening fluid to form a shear layer in the rim region. As the droplet recedes and then elongates, the two-prong structure also develops as a result of the intensive axial stretch from the shear-thinning fluid. As illustrated in Fig. 12, the mixing intensity for $\mathrm{We} = 200$ is significantly larger than that in the stage of droplet radial expansion as well as subsequent stages. This result indicates that the two-prong structure increases the liquid-liquid contact area and thereby enhances mixing during the radial recession and axial elongation stages.

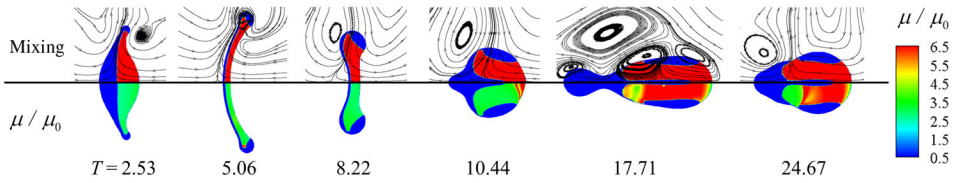

FIG. 11. Evolution of the flow field and the normalized viscosity distribution of case (d) in Fig. 10.

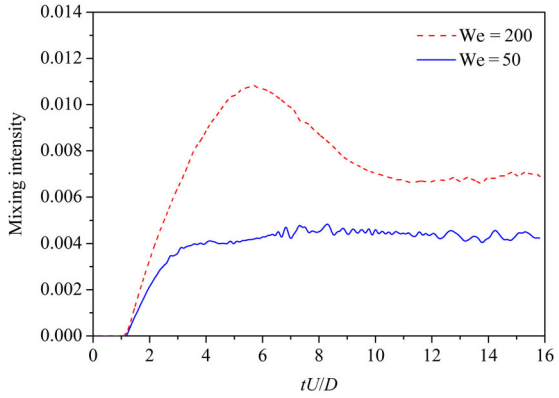

FIG. 12. Comparison of the mixing intensity between the cases We = 50 and We = 200 in Fig. 10.

IV. CONCLUDING REMARKS

The head-on collision between equal-sized droplets of non-Newtonian fluids is computationally studied by using the lattice Boltzmann method coupled with tracking massless particles in the droplets by using the fourth-order Runge-Kutta method, and employing the Carreau-Yasuda model and a piecewise function to describe the shear-thinning and shear-thickening effects, respectively.

The shear-thinning fluids, whose viscosity is usually high at a zero shear rate, while it decreases with an increasing local shear rate, show a complex influence on the droplet dynamics in terms of coalescence and separation and internal mixing. If the extent of shear thinning is small, identical shear-thinning droplets behave similar to their Newtonian counterparts with a larger effective viscosity, and are not likely to separate due to the increased viscous loss and hence reduced kinetic energy of the internal motion. However, unbalanced large-scale internal motion can be generated when the droplets are of an unequal extent of shear thinning, and will persist within the child droplets produced upon separation of the merged mass due to the difference in the reduced viscous loss. The prevalence of such internal motion promotes mixing. For shear-thickening fluids, results show that the increased viscous loss suppresses droplet separation, as expected, and as such affords extended duration for internal mixing.

With the understanding that the disparity in non-Newtonian flow effect can break the symmetry of equal-size droplets with identical physical properties, and that the shear-thickening effect induces high viscous dissipation, the collision between a strong shear-thinning droplet and a strong shear-thickening droplet is found to simultaneously enhance mixing and suppress separation. Rich phenomena of droplet mixing are observed, including either partial or complete wrapping of the shear-thickening fluid by the shear-thinning fluid, depending on the Weber number.

The present results are expected to be of value in designing GHP propulsion systems as well as various ink-jet printing systems whose performance largely relies on the mixing of discrete liquid phases. Specifically, a few design suggestions can be made to promote the ignition stability of GHP rocket engines: (i) Highly shear-thinning propellants are not favored since the coalesced fuel-oxidizer droplets of a strong shear-thinning effect tend to separate easily. (ii) Shear-thickening propellants may be of value for droplet collisions with a large-impact inertia since they tend to suppress droplet separation while the impact inertia promotes it. (iii) disparity in the non-Newtonian rheology between the fuel and the oxidizer, through either gelling them with a different extent of shear thinning, or gelling one of them for shear thinning while the other for shear thickening, may improve the internal mixing.

ACKNOWLEDGMENTS

The visit of Kai Sun to Princeton University was supported by the China Scholarship Council (No. 201406250099). The work at the Hong Kong Polytechnic University was supported by the Hong Kong Research Grants Council/General Research Fund (operating under Contract No. PolyU 152217/14E). The collaboration between the Hong Kong Polytechnic University and Tsinghua University was facilitated through the SRFDP & RGC ERG Joint Research Scheme (M-PolyU509/13). The work at Princeton University was supported in part by a gift grant from the Xerox Corporation.

[1] P. R. Brazier-Smith, S. G. Jennings, and J. Latham, The interaction of falling water drops: Coalescence, Proc. R. Soc. A **326**, 393 (1972).
[2] N. Ashgriz and J. Y. Poo, Coalescence and separation in binary collisions of liquid drops, J. Fluid Mech. **221**, 183 (1990).
[3] J. Qian and C. K. Law, Regimes of coalescence and separation in droplet collision, J. Fluid Mech. **331**, 59 (1997).
[4] K. D. Willis and M. E. Orme, Binary droplet collisions in a vacuum environment: An experimental investigation of the role of viscosity, Exp. Fluids **29**, 347 (2000).
[5] K. L. Pan, C. K. Law, and B. Zhou, Experimental and mechanistic description of merging and bouncing in head-on binary droplet collision, J. Appl. Phys. **103**, 064901 (2008).
[6] K. L. Pan, P. C. Chou, and Y. J. Tseng, Binary droplet collision at high Weber number, Phys. Rev. E **80**, 036301 (2009).
[7] C. L. Tang, P. Zhang, and C. K. Law, Bouncing, coalescence, and separation in head-on collision of unequal-size droplets, Phys. Fluids **24**, 022101 (2012).
[8] N. Nikolopoulos, K. S. Nikas, and G. Bergeles, A numerical investigation of central binary collision of droplets, Comput. Fluids **38**, 1191 (2009).
[9] K. Sun, M. Jia, and T. Y. Wang, Numerical investigation of head-on droplet collision with lattice Boltzmann method, Int. J. Heat Mass Transfer **58**, 260 (2013).

[10] D. Lycett-Brown, K. H. Luo, R. H. Liu, and P. M. Lv, Binary droplet collision simulations by a multiphase cascaded lattice Boltzmann method, Phys. Fluids **26**, 023303 (2014).

[11] C. K. Kuan, K. L. Pan, and W. Shyy, Study on high-Weber-number droplet collision by a parallel, adaptive interface-tracking method, J. Fluid Mech. **759**, 104 (2014).

[12] P. Zhang and C. K. Law, An analysis of head-on droplet collision with large deformation in gaseous medium, Phys. Fluids **23**, 042102 (2011).

[13] I. V. Roisman, Dynamics of inertia dominated binary drop collisions, Phys. Fluids **16**, 3438 (2004).

[14] A. Gopinath and D. L. Koch, Collision and rebound of small droplets in an incompressible continuum gas, J. Fluid Mech. **454**, 145 (2002).

[15] G. A. Bach, D. L. Koch, and A. Gopinath, Coalescence and bouncing of small aerosol droplets, J. Fluid Mech. **518**, 157 (1999).

[16] A. V. Anilkumar, C. P. Lee, and T. G. Tang, Surface-tension-induced mixing following coalescence of initially stationary drops, Phys. Fluids A **3**, 2587 (1991).

[17] N. Nikolopoulos and G. Bergeles, The effect of gas and liquid properties and droplet size ratio on the central collision between two unequal-size droplets in the reflexive regime, Int. J. Heat Mass Transfer **54**, 678 (2011).

[18] D. Liu, P. Zhang, C. K. Law, and Y. C. Guo, Collision dynamics and mixing of unequal-size droplets, Int. J. Heat Mass Transfer **57**, 421 (2013).

[19] K. Sun, M. Jia, and T. Y. Wang, Numerical investigation on the head-on collision between unequal-sized droplets with multiple-relaxation-time lattice Boltzmann model, Int. J. Heat Mass Transfer **70**, 629 (2014).

[20] C. L. Tang, P. Zhang, C. K. Law, and Z. H. Huang, Dynamics of internal jet in the mixing of droplets of unequal sizes, in revision.

[21] F. Blanchette, Simulation of Mixing within Drops Due to Surface Tension Variations, Phys. Rev. Lett. **105**, 074501 (2010).

[22] C. Focke, M. Kuschel, M. Sommerfeld, and D. Bothe, Collision between high and low viscosity droplets: Direct numerical simulations and experiments, Int. J. Multiphase Flow **56**, 81 (2013).

[23] H. Minemawari, T. Yamada, H. Matsui, J. Tsutsumi, S. Haas, R. Chiba, R. Kumai, and T. Hasegawa, Inkjet printing of single-crystal films, Nature (London) **475**, 364 (2011).

[24] S. Fathi and P. Dickens, Challenges in drop-on-drop deposition of reactive molten nylon materials for additive manufacturing, J. Mater. Process. Technol. **213**, 84 (2013).

[25] E. M. Dambach, K. Y. Cho, T. L. Pourpoint, and S. D. Heister, Ignition of advanced hypergolic propellants, in Proceedings of the 46th AIAA/ASME/SAE/ASEE Joint Propulsion Conference & Exhibit, Nashville, 2010 (unpublished).

[26] C. K. Law, Fuel options for next-generation chemical propulsion, AIAA J. **50**, 19 (2012).

[27] A. M. Nightingale, T. W. Phillips, J. H. Bannock, and J. C. de Mello, Controlled multistep synthesis in a three-phase droplet reactor, Nat. Commun. **5**, 3777 (2014).

[28] A. B. Theberge, E. Mayot, A. E. Harrak, F. Kleinschmidt, W. T. S. Huck, and A. D. Griffiths, Microfluidic platform for combinatorial synthesis in picolitre droplets, Lab Chip **12**, 1320 (2012).

[29] G. Brenn in *Handbook of Atomization and Sprays*, edited by N. Ashgriz (Springer, New York, 2011).

[30] M. Motzigemba, N. Roth, D. Bothe, H. J. Warnecke, J. Prüss, K. Wielage, and B. Weigan, The effect of non-Newtonian flow behavior on binary droplet collisions: VOF-simulation and experimental analysis, in Proceedings of the 18th Annual Conference Liquid Atomization and Spray Systems (ILASS-Europe), Zaragoza, 2002(unpublished).

[31] C. Focke and D. Bothe, Computational analysis of binary collisions of shear-thinning droplets, J. Non-Newtonian Fluid Mech. **166**, 799 (2011).

[32] C. Focke and D. Bothe, Direct numerical simulation of binary off-center collision of shear thinning droplets at high Weber numbers, Phys. Fluids **24**, 073105 (2012).

[33] K. Sun, T. Wang, P. Zhang, and C. K. Law, Non-Newtonian flow effects on the coalescence and mixing of initially stationary droplets of shear-thinning fluids, Phys. Rev. E **91**, 023009 (2015).

[34] R. Benzi, S. Succi, and M. Vergassol, The lattice Boltzmann equation: Theory and applications, Phys. Rep. **222**, 145 (1992).

[35] S. Chen and G. D. Doolen, Lattice Boltzmann methods for fluid flows, Annu. Rev. Fluid Mech. **30**, 329 (1998).

[36] M. Sbragaglia, R. Benzi, L. Biferale, S. Succi, K. Sugiyama, and F. Toschi, Generalized lattice Boltzmann method with multirange pseudopotential, Phys. Rev. E **75**, 026702 (2007).

[37] G. Falcucci, G. Bella, G. Chiatti, S. Chibbaro, M. Sbragaglia, and S. Succi, Lattice Boltzmann models with mid-range interactions, Commun. Comput. Phys. **2**, 1071 (2007).

[38] H. W. Zheng, C. Shu, and Y. T. Chew, A lattice Boltzmann model for multiphase flows with large density ratio, J. Comput. Phys. **218**, 353 (2006).

[39] T. Lee and L. Liu, Lattice Boltzmann simulations of micron-scale drop impact on dry surfaces, J. Comput. Phys. **229**, 8045 (2010).

[40] T. Lee, Effects of incompressibility on the elimination of parasitic currents in the lattice Boltzmann equation method for binary fluids, Comput. Math. Appl. **58**, 987 (2009).

[41] M. P. Escudier, I. W. Gouldson, A. S. Pereira, F. T. Pinho, and R. J. Pool, On the reproducibility of the rheology of shear-thinning liquids, J. Non-Newtonian Fluid Mech. **97**, 99 (2001).

[42] F. J. Galindo-Rosales, F. J. Rubio-Hernández, and A. Sevill, An apparent viscosity function for shear thickening fluids, J. Non-Newtonian Fluid Mech. **166**, 321 (2011).

[43] P. T. Yue, J. J. Feng, C. Liu, and J. Shen, A diffuse-interface method for simulating two-phase flows of complex fluids, J. Fluid Mech. **515**, 293 (2004).

[44] J. J. Feng, C. Liu, J. Shen, and P. T. Yue, in *Modeling of Soft Matter (IMA Volumes in Mathematics and its Applications)*, edited by M.-C. T. Calderer and E. Terentjev (Springer, New York, 2005).

[45] D. Chiappini, G. Bella, S. Succi, F. Toschi, and S. Ubertini, Improved lattice Boltzmann without parasitic currents for Rayleigh-Taylor instability, Commun. Comput. Phys. **7**, 423 (2010).

[46] A. Kukukova, J. Aubin, and S. M. Kresta, A new definition of mixing and segregation: Three dimensions of a key process variable, Chem. Eng. Res. Des. **87**, 633 (2009).